Prepared for submission to JINST

21TH International Workshop on Radiation Imaging Detectors
7-12 July 2019
Kolympari, Chania, Crete, Greece

Effectiveness of X-ray phase-contrast tomography: effects of pixel size and magnification on image noise

L. Brombal,[a,b,1]

[a] *University of Trieste, Department of Physics, via A. Valerio 2, 34100, Trieste, Italy*
[b] *INFN, Division of Trieste, via A. Valerio 2, 34100, Trieste, Italy*

E-mail: luca.brombal@ts.infn.it

Abstract: Noise magnitude in conventional attenuation X-ray tomography (CT) is strongly dependent on the pixel size and/or the geometrical magnification, thereby limiting the possibility of achieving high-resolution low-dose CT imaging. In this context, the use of Propagation-Based Imaging (PBI) phase-contrast technique coupled with the application of a suitable Phase-Retrieval (PhR) filter is a valuable tool to overcome such limitation. In fact, at fixed radiation dose, the noise dependence on the effective pixel size when the PhR filter is applied is much shallower with respect to conventional CT imaging. Making use of a theoretical framework developed by other authors, this work demonstrates quantitatively the dependence of CT image noise on pixel size and magnification in PBI. Calculations are compared with experimental images of a breast specimen imaged at the SYRMEP beamline at the Elettra synchrotron facility (Trieste, Italy), with a CdTe photon-counting detector in PBI configuration. The results, expressed in terms of Signal-to-Noise Ratio (SNR) gain due to the PhR application, show a good agreement between predictions and experimental data at all pixel pitches and magnifications, quantitatively demonstrating the importance of going towards detectors featuring smaller pixels (or higher spatial resolution) to fully exploit the advantages of PBI and PhR. Specifically, SNR gain up to a factor of 20 is observed at the smallest pixel pitch (60 μm) and largest magnification (1.40). At the same time, as predicted theoretically, larger magnifications correspond to lower image noise (or higher SNR) when PhR is applied: this trend is unparalleled in attenuation-based CT imaging where larger magnifications, hence smaller effective pixel sizes, lead to a higher noise.

Keywords: Computerized Tomography (CT), Models and simulations, Hybrid detectors, X-ray detectors, Data processing methods

[1]Corresponding author.

Contents

1 Introduction

Noise magnitude in conventional attenuation-based X-ray tomographic (CT) imaging is strongly dependent on the detector pixel size and/or the geometrical magnification. For this reason, when constraints in terms of radiation dose or scan time are present, as in clinical or animal studies, high-resolution CT imaging at acceptable noise levels is not feasible. This is especially true when imaging light (low-Z) samples, as soft tissues, where the small attenuation contrast signal between different features of the sample is easily buried under image noise.

In this context, the use of X-ray Phase-Contrast Imaging (XPCI) techniques is a powerful tool to increase detail visibility within soft tissues. XPCI relies on the real decrement (δ) of the refractive index (n), responsible for X-ray phase effects, whereas conventional imaging is based on its imaginary part (β), proportional to the X-ray linear attenuation coefficient: for light materials in the energy range of radiological interest (10-100 keV), δ is two to three orders of magnitude larger β, thus phase effects are larger than attenuation [1].

Among XPCI techniques, Propagation-Based Imaging (PBI) is arguably the simplest to implement as it only requires to introduce some (propagation) distance between sample and detector. On the contrary, to effectively detect phase effects, PBI has strict requirements in terms of spatial coherence of the X-rays incident onto the sample (X-ray source must be small or distant from the sample). For this reason, the use of PBI has been mostly limited to Synchrotron Radiation (SR) facilities or laboratory microfocal sources even if applications with conventional high-power X-ray tubes exist [2, 3]. The main difference between a conventional attenuation and a PBI image is the presence of a phase-contrast signal arising at the interfaces between different structures of the sample in the form of dark/bright fringes [4]. This effect, referred to as edge-enhancement, can be modelled as a high-spatial frequency boost in Fourier space hence, effectively, as an increase in the spatial resolution [5]. In CT applications it is common to further process PBI projection images by applying a Phase-Retrieval (PhR) algorithm: the most widely single-shot PhR method is based on the Homogeneous Transport-of-Intensity Equation (TIE-Hom), assuming the imaged object to have a constant (and known) δ/β ratio [6]. It has been shown, both theoretically and experimentally, that

the application of TIE-Hom PhR on PBI images results in images whose content is proportional (up to a logarithmic transformation) to conventional (attenuation-based) images but with a significant noise reduction [5, 7, 8]. Intuitively, this can be understood considering that the PhR acts as a low-pass filter exactly compensating for the high spatial frequency boost due to the propagation but, at the same time, bringing to a major decrease in image noise or, equivalently, to an increase of Signal-to-Noise Ratio (SNR). The effect of PhR on CT image noise has been mathematically described by a thorough model proposed by Nesterets and collaborators including all the components in the imaging chain, from the geometrical configuration of the setup and detector's characteristics to the tomographic reconstruction [9, 10]. Specifically, the model shows that the application of PhR strongly mitigates the noise dependence on the (effective) pixel size. Moreover, smaller pixel sizes and/or larger geometrical magnifications correspond to a larger noise reduction due to the PhR, thus amplifying the difference between images reconstructed with or without PhR.

In addition to PBI, biomedical imaging can take advantage of high-Z direct-conversion photon-counting detectors, which offer high efficiency and Poisson dominated noise [11]. Moreover, unlike indirect-conversion devices where the intermediate conversion stage usually introduces some blurring, the spatial response function of these detectors is usually dominated by the pixel size (aperture). These features allow to make use of several simplifications in the aforementioned model.

In this work PBI tomographic images of a surgical breast specimen are analyzed and compared with the described theoretical model focusing on the effects of pixel size and geometrical magnification. The measurements have been performed at the Italian synchrotron radiation facility Elettra (Trieste, Italy), within the framework of the SYRMA-3D project, which aims at performing in-vivo PBI breast CT at the SYRMEP beamline [12]. Images are obtained by using a large-area CdTe photon-counting detector (Pixirad-8), featuring 60 μm pixel pitch and 650 μm sensor thickness, thus ensuring a nearly total absorption efficiency at the selected beam energy (30 keV) [13]. In addition to the native pixel spacing, the acquired projections have been rebinned to simulate pixel pitches up to 240 μm and the sample has been imaged at three magnifications.

2 Materials and Methods

2.1 CT image noise model

By assuming a Poisson dominated detector noise, flat-fielded bi-dimensional projection images (divided by nearly noise-free projections collected with no sample in the beam), stable source intensity and imaging setup, and parallel beam tomographic reconstruction performed through the Filtered-Back-Projection (FBP) algorithm, the variance (var) in a region of a CT image featuring an homogeneous attenuation coefficient is [10]:

$$\mathrm{var} = \frac{f(A; d/h) F_{\mathrm{obj}}}{N_p (h/M)^4 \Phi \mathrm{DQE}_0 T_{\mathrm{gap}}} \tag{2.1}$$

where F_{obj} accounts for X-rays attenuation in the object, N_p is the number of projections in the tomographic scan, Φ is the X-ray fluence at the object (in number of photons per square millimeter), DQE_0 is the detector quantum efficiency at zero spatial frequency, T_{gap} is the transmittance of the gap (usually composed by air) between sample and detector, M is the geometrical magnification

and h is the physical size of a detector pixel, which is assumed to be bi-dimensional with equal width and height. The dimensionless function $f(A; d/h)$ accounts for the tomographic process, the detector response and the phase retrieval, and it is written as:

$$f(A; d/h) = 2\pi^2 \int_0^{\frac{1}{2}} \mathrm{d}U G^2(U) F_{\mathrm{interp}}(U) \int_{-\frac{1}{2}}^{\frac{1}{2}} \mathrm{d}V \frac{\mathrm{MTF}^2(U, V; d/h)}{\left[1 + A\left(U^2 + V^2\right)\right]^2} \tag{2.2}$$

Here $G(U)$ is the CT filter, $F_{\mathrm{interp}}(U)$ describes the effect on noise of the interpolation from polar to Cartesian coordinates in the backprojection process, $\mathrm{MTF}(U, V; d/h)$ is the detector modulation transfer function parametrized through the dimensionless quantity d/h, where d is the Full Width at Half Maximum (FWHM) of the detector's Point Spread Function (PSF). Of note, the integration variables U and V are dimensionless normalized frequencies expressing the fractions of twice the maximum detected frequency (Nyquist frequency), hence the fractions of $(h/M)^{-1}$. Finally, the dimensionless parameter A depends on the refractive properties of the sample, on the setup geometry and on the detector pixel size as

$$A = \pi \frac{\delta_1 - \delta_2}{\beta_1 - \beta_2} \lambda R_1 M(M-1)/h^2 \tag{2.3}$$

λ being the radiation wavelength and the subscripts 1, 2 in the δ and β terms refer to an interface between two materials having given different refractive indices (two-materials PhR) [14].

Despite its rather complex formulation, the function f is key in understanding the effect of phase retrieval on image noise which is given by the denominator of the last term in equation (2.2). In facts, when no PhR is applied $A = 0$ and, as a consequence, the function f does not explicitly depend neither on the pixel size h nor on the magnification M: in this case, as reported in equation (2.1), the image noise ($\sigma = \sqrt{\mathrm{var}}$) is found to be proportional to M^2/h^2, which is a known result in the context of conventional CT. This strong dependence of image noise on pixel size and magnification quantitatively explains why low-dose high-resolution images with acceptable noise levels cannot be obtained. On the contrary, if PhR is applied $A > 0$ and the denominator in equation (2.2) is larger than 1, hence the function f gets smaller if compared with the case $A = 0$, bringing to a reduction of image noise. More in detail, according to equation (2.3), a decrease in the pixel size and/or an increase in geometrical magnification, bring to an increase of the parameter A that determines a larger noise reduction due to PhR. In this perspective, PhR applied to PBI projections strongly mitigates the pixel size and magnification dependence of image noise, opening up the possibility of low-dose high-resolution CT imaging. Importantly, TIE-Hom PhR can be applied to images acquired in the near-field propagation regime, corresponding to large Fresnel numbers ($N_F = h^2/(M^2 \lambda R_2) > 1$), which means that the parameter A cannot become indefinitely large and, therefore, the noise cannot be indefinitely small.

2.2 Experimental setup and data processing

To test the model against experimental results, tomographic images of a single mastectomy specimen containing cancer (diameter of about 10 cm) has been reconstructed from 1200 projections evenly spaced over 180 degrees acquired in continuous rotation mode resulting in an overall exposure of 40 s. The Directive 2004/23/EC of the European Parliament and of the Council of 31 March

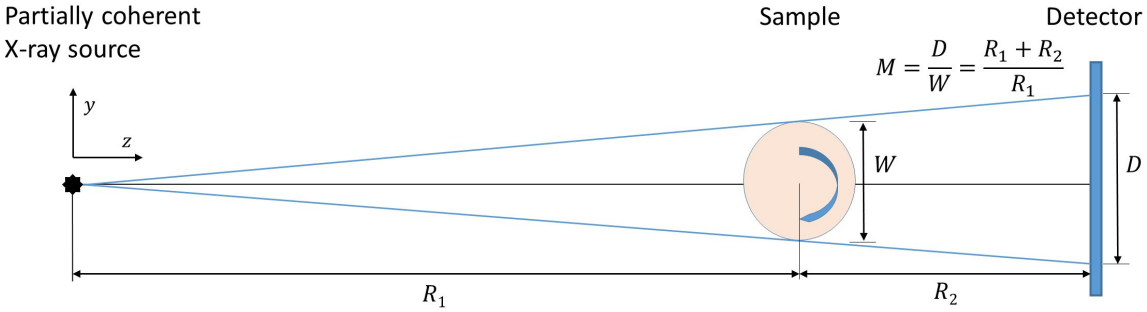

Figure 1. Sketch of the propagation based imaging experimental setup. R_1 is the source-to-sample distance, R_2 is the sample-to-detector distance, W is the sample dimension and D is the sample dimension projected on the detector. From both D, W and R_1, R_2 the geometrical magnification M can be determined. The drawing is not to scale.

2004 on setting standards of quality and safety for the donation, procurement, testing, processing, preservation, storage and distribution of human tissues were followed. The scans were performed at the SYRMEP beamline of the Elettra synchrotron facility, where the X-ray beam is produced by one storage ring bending magnet and the energy was fixed to 30 keV by means of a Si(111) double-crystal monochromator, providing an effective energy resolution of 0.1 %. Projection images are collected with a large-area (246×24.8 mm^2) CdTe photon-counting detector featuring a native pixel pitch of 60 μm ensuring a nearly total X-ray absorption efficiency up to 40 keV. The detector is operated in dead-time-free mode with the maximum available frame rate of 30 Hz, and it is placed at a fixed distance from the source $R_1+R_2 = 31.6$ m, as sketched in figure 1. Once acquired, projection images are fed to a detector-specific pre-processing procedure and optionally phase-retrieved considering a glandular/adipose interface corresponding to $(\delta_1 - \delta_2)/(\beta_1 - \beta_2) = 795$ [15]. CT images are reconstructed via a GPU-based parallel-beam FBP with a Shepp-Logan filter, meaning that, in the model introduced in the previous section, $G(U) = U\,\mathrm{sinc}(U)$ where $\mathrm{sinc}(U) = \sin(\pi x)/(\pi x)$ is the normalized sinc function. The backprojection algorithm makes use of linear interpolation, therefore $F_{\mathrm{interp}}(U) = [2 + \cos(2\pi U)]/3$. The detector MTF is modelled as a bi-dimensional sinc function $\mathrm{MTF}(U, V; 1) = \mathrm{sinc}(U)\,\mathrm{sinc}(V)$, which implies a bi-dimensional box-shaped PSF having a width corresponding to the pixel size. The latter assumption, despite being an approximation, is rather reasonable for photon-counting detectors as Pixirad-8, where the PSF width is dominated by the physical pixel dimension, hence $d/h \simeq 1$. Moreover, this approximation allows to simulate different physical pixel sizes simply by rebinning projection images without changing the functional form of MTF in equation (2.2). Specifically, the acquired projections have been rebinned to yield a set of pixel sizes $h = [60\ \mu\mathrm{m}, 120\ \mu\mathrm{m}, 180\ \mu\mathrm{m}, 240\ \mu\mathrm{m}]$. The sample has been scanned at 3 different propagation distances corresponding to source-to-sample distances $R_1 = [30.0\ \mathrm{m}, 28.6\ \mathrm{m}, 22.6\ \mathrm{m}]$ and magnification factors $M = [1.05, 1.10, 1.40]$. The photon fluence was tuned to deliver 25 mGy of mean glandular dose at the patient support position (corresponding to $R_1 = 30$ m, M =1.05) and kept fixed to have constant statistics at the detector [7].

For each image, reconstructed both with and without applying PhR, the SNR has been measured

within an homogeneous fibroglandular region as

$$SNR = \frac{\langle I \rangle}{\sigma} \tag{2.4}$$

where $\langle I \rangle$ is the average gray level of a circular region-of-interest (ROI) and σ is the standard deviation within the same ROI. Starting from the measured SNR values, for each pixel dimension and magnification factor, the SNR gain factor (or noise decrease factor) has been computed as

$$SNR_{\text{gain}} = \frac{\sigma_{\text{noPhR}}}{\sigma_{\text{PhR}}} = \frac{SNR_{\text{PhR}}}{SNR_{\text{noPhR}}} \tag{2.5}$$

where the subscripts refer to images without (noPhR) and with (PhR) phase retrieval. Of note, even if the delivered mean glandular dose is higher than the SYRMA-3D clinical target (5 mGy or below) [12], the SNR gain factor does not depend from the absolute dose value as the fluence term appearing in equation (2.1) cancels out when taking the ratio of image noise levels (or, equivalently, of signal-to-noise ratios). Therefore, the experimental results expressed in terms of SNR gain in the next section have a rather general validity, regardless the absolute dose value.

3 Results and discussion

Figure 2 shows a detail of the breast specimen sample enclosing a fibroglandular detail (bright gray) embedded in an adipose background (dark gray) acquired at R_1 = 22.6 m, M = 1.40, and reconstructed with four different pixel sizes (by columns), without and with the PhR (by rows). As expected, considering the images without PhR, the pixel size plays an important role in terms of image noise and a dramatic noise increase is associated with the native pixel spacing (60μm) when compared with the largest pixel size (240μm). At the same time the use of larger pixel sizes obviously result in an increased image blurring (or loss of spatial resolution) which greatly reduces the visibility of the edge-enhancement effect. Conversely, the image noise dependence on the pixel size is way less pronounced in case of phase-retrieved images, as predicted by the aforementioned model, whereas the most evident effect is the image blurring associated to larger pixel sizes.

The plots in figure 3 report, quantitatively, the model results and their comparison with the experimental measurements. Specifically, panel (a) shows the predicted noise dependence on the pixel size for all the geometrical configurations (R_1, M) considering a fixed fluence level at the sample, hence fixed dose. If no phase retrieval is applied (dashed lines), as in conventional imaging, image noise is described by the power law $\sigma \propto h^{-2}$, and larger magnifications are associated to higher image noise at all pixel sizes. This is partly because larger magnifications result in smaller effective pixel sizes (h/M) and partly because large magnifications are related to large propagation distances (R_2) hence to a higher air attenuation between sample and detector. On the other hand, when phase retrieval is applied (solid lines) image noise asymptotically converges to the values predicted for non phase-retrieved images at large pixel sizes, as $A \propto h^{-2}$ becomes small, but show a much shallower dependence on the pixel dimension. In particular, for smaller pixel sizes the noise difference between phase retrieved and non-phase retrieved data dramatically increases or, in other terms, the noise reduction factor due to phase retrieval largely increases. Of note, in the geometrical configurations reported in this study, larger magnifications yield smaller image noise at smaller

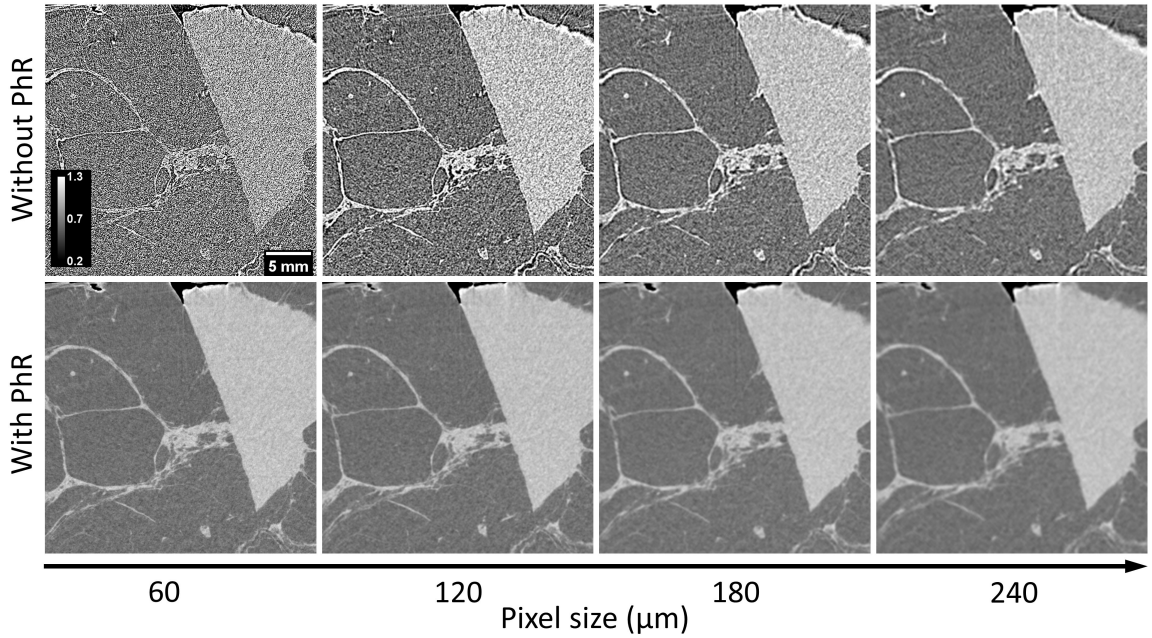

Figure 2. Crop of a reconstructed tomographic slice showing a fibroglandular detail embedded in adipose background acquired at R_1 = 22.6 m, M = 1.40. Each column refers to a given pixel size while each row specifies whether the PhR is applied or not. All the images are windowed on the same gray level scale (inset of the top-left image) to facilitate the comparison. The sharp interface between the two tissues is produced by a surgical cut.

pixel sizes whereas, if the detector pixel size is large ($\gtrsim 300\mu$m), smaller magnifications should be preferred. This can be explained considering that for large pixel sizes phase retrieval does not affect much image noise, which is therefore dominated by the term M^2/h^2 as in conventional (non-phase retrieved) images.

In panel (b) the SNR gain predicted by the model (lines, resulting from the ratio of the curves displayed in panel (a)) and measured from experimental images (points) is reported as a function of the pixel size. From the plot it is clear that the model well describes experimental data for all the geometrical configurations, therefore being a powerful tool for estimating the effect of phase retrieval on image noise. Specifically, at the native pixel spacing of 60μm the SNR gain goes up to a factor larger than 20 when considering the largest geometrical magnification. Conversely, as expected, smaller SNR gain is found at larger pixel size and the curves converge asymptotically to the value of 1 (no gain).

So far, mostly image noise and SNR dependence on detector pixel size have been discussed. Anyway, the model can be of use in understanding and optimizing the geometrical configuration of an experimental setup which includes a detector of a given pixel size. In figure 4 the predicted image noise (color scale) for a detector with pixel size of 60 μm at constant sample fluence is plotted as a function of the source-to-sample distance (R_1) and magnification (M) in case of no PhR, panel (a), and considering the PhR, panel (b). In the first case, representing conventional CT, the image noise is strongly dependent and monotonically increasing with the magnification ($\propto M^2$), whereas source-to-sample distance plays a little role at low magnifications and it becomes more important at

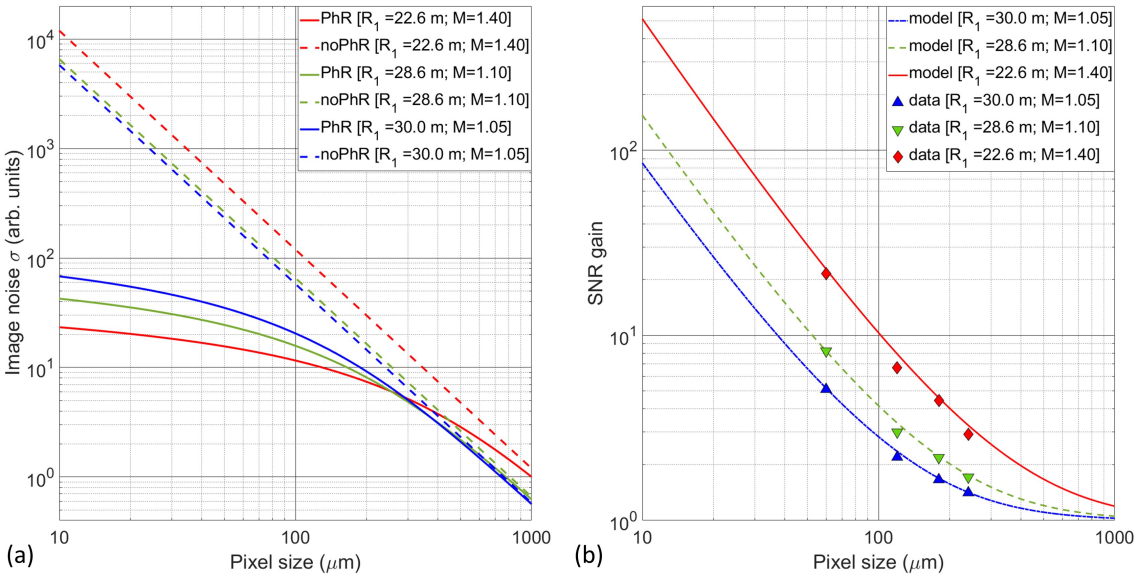

Figure 3. In (a) the predicted image noise as a function of the pixel size for both cases with (solid lines) and without (dashed lines) PhR and all geometric configurations. In (b) the predicted (lines) and measured (points) SNR gain due to the application of PhR in all geometrical configurations.

large magnifications due to photon attenuation (large R_1 and M means large R_2, hence lower photon transmission between sample and detector). When PhR is applied the plot changes dramatically, and the noise is found to decrease at larger magnification and source-to-sample distance. This trend is unparalleled in conventional CT and it can be intuitively explained considering that large propagation distances (R_2), which are related to large values of R_1 and M, lead to stronger phase-effects and, in turn, to a more effective phase retrieval. As a general remark, since the model hereby described holds in the 'near-field' approximation, noise cannot arbitrarily decreased and, as a first line discrimination, only results corresponding to Fresnel numbers larger than 1 should be considered.

4 Conclusions

Based on a theoretical model proposed by other authors, this work shows experimentally that the use of detector featuring a small pixel size and pixel-aperture dominated response function is key to take advantage of the noise reduction properties of the phase-retrieval algorithm. In fact, the much shallower dependence of CT image noise on pixel size in phase-retrieved images enables, by using the propagation-based phase-contrast configuration, high-resolution low-dose CT imaging. Specifically, having included the realistic geometry of a synchrotron-based breast CT clinical project and the detector response of the used photon-counting device, the model accurately predicts the effect of phase retrieval on signal-to-noise-ratio for different pixel sizes and geometrical magnifications. In this context, an extensive use of this model can be a powerful tool to design and optimize any propagation-based imaging experiment where the noise performances are critical.

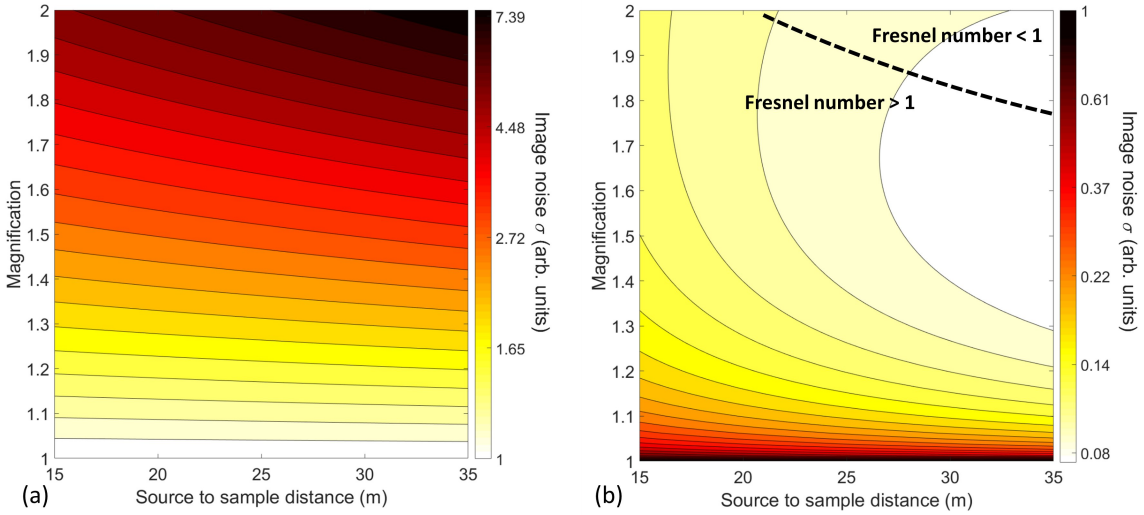

Figure 4. Predicted image noise (color bar) as a function of source-to-sample distance (R_1) and magnification (M) for images without (a) and with (b) PhR.

Acknowledgments

The author gratefully acknowledges all the members of the SYRMA-3D collaboration and sincerely thanks Dr Luigi Rigon for his help in reviewing the manuscript. SYRMA-3D project is supported by Istituto Nazionale di Fisica Nucleare (National Scientific Commission 5 for Technological and Inter-disciplinary Research) and Elettra Sincrotrone Trieste S.C.p.A.

References

[1] A. Bravin et al. X-ray phase-contrast imaging: from pre-clinical applications towards clinics. *Physics in Medicine & Biology*, 58(1):R1, 2012. doi: https://doi.org/10.1088/0031-9155/58/1/R1.

[2] A. Olivo and E Castelli. X-ray phase contrast imaging: From synchrotrons to conventional sources. *Rivista del nuovo cimento*, 37(9):467–508, 2014. doi: https://doi.org/10.1393/ncr/i2014-10104-8.

[3] L. Brombal et al. Monochromatic Propagation-Based Phase-Contrast Microscale Computed-Tomography System with a Rotating-Anode Source. *Physical Review Applied*, 11(3): 034004, 2019. doi: https://doi.org/10.1103/PhysRevApplied.11.034004.

[4] S. W. Wilkins et al. Phase-contrast imaging using polychromatic hard x-rays. *Nature*, 384(6607):335, 1996. doi: https://doi.org/10.1038/384335a0.

[5] T. E. Gureyev et al. On the “unreasonable” effectiveness of transport of intensity imaging and optical deconvolution. *JOSA A*, 34(12):2251–2260, 2017. doi: https://doi.org/10.1364/JOSAA.34.002251.

[6] D. Paganin et al. Simultaneous phase and amplitude extraction from a single defocused image of a homogeneous object. *Journal of microscopy*, 206(1):33–40, 2002. doi: https://doi.org/10.1046/j.1365-2818.2002.01010.x.

[7] L. Brombal et al. Phase-contrast breast ct: the effect of propagation distance. *Physics in Medicine & Biology*, 63(24):24NT03, 2018. doi: https://doi.org/10.1088/1361-6560/aaf2e1.

[8] A. Piai et al. Quantitative characterization of breast tissues with dedicated CT imaging. *Physics in Medicine & Biology*, 64(15):155011, 2019. doi: https://doi.org/10.1088/1361-6560/ab2c29.

[9] Y. I. Nesterets and T. E. Gureyev. Noise propagation in x-ray phase-contrast imaging and computed tomography. *Journal of Physics D: Applied Physics*, 47(10):105402, 2014. doi: https://doi.org/10.1088/0022-3727/47/10/105402.

[10] Y. I. Nesterets et al. Optimisation of a propagation-based x-ray phase-contrast micro-CT system. *Journal of Physics D: Applied Physics*, 51(11):115402, 2018. doi: https://doi.org/10.1088/1361-6463/aaacee.

[11] R. Ballabriga et al. Review of hybrid pixel detector readout ASICs for spectroscopic X-ray imaging. *Journal of Instrumentation*, 11(01):P01007, 2016.

[12] R. Longo et al. Advancements towards the implementation of clinical phase-contrast breast computed tomography at Elettra. *Journal of Synchrotron Radiation*, 26(4), 2019. doi: https://doi.org/10.1107/S1600577519005502.

[13] R. Bellazzini et al. Chromatic x-ray imaging with a fine pitch cdte sensor coupled to a large area photon counting pixel asic. *Journal of Instrumentation*, 8(02):C02028, 2013. doi: https://doi.org/10.1088/1748-0221/11/01/P01007.

[14] A. Burvall et al. Phase retrieval in x-ray phase-contrast imaging suitable for tomography. *Optics express*, 19(11):10359–10376, 2011. doi: https://doi.org/10.1364/OE.19.010359.

[15] L. Brombal et al. Large-area single-photon-counting CdTe detector for synchrotron radiation computed tomography: a dedicated pre-processing procedure. *Journal of Synchrotron Radiation*, 25 (4), 2018. doi: https://doi.org/10.1107/S1600577518006197.